Urban Climate 49 (2023) 101455

Contents lists available at ScienceDirect

Urban Climate

journal homepage: www.elsevier.com/locate/uclim

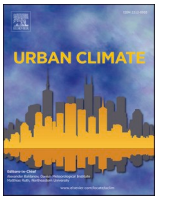

Exploring the seasonality of surface urban heat islands using enhanced land surface temperature in a semi-arid city

Liying Han [a,b,c], Linlin Lu [a,b,*], Peng Fu [d], Chao Ren [e], Meng Cai [f], Qingting Li [g]

[a] Key Laboratory of Digital Earth Science, Aerospace Information Research Institute, Chinese Academy of Sciences, Beijing, China
[b] International Research Center of Big Data for Sustainable Development Goals, Beijing, China
[c] College of Geological Engineering and Geomatics, Chang'an University, Xi'an, China
[d] Centre for Environment, Energy, and Economy, Harrisburg University of Science and Technology, Harrisburg, PA, USA
[e] Faculty of Architecture, The University of Hong Kong, Hong Kong, China
[f] School of Architecture, The Chinese University of Hong Kong, Hong Kong, China
[g] Airborne Remote Sensing Center, Aerospace Information Research Institute, Chinese Academy of Sciences, Beijing, China

ARTICLE INFO

Keywords:
Local climate zone
Land surface temperature
Data fusion
Seasonal hysteresis
Surface urban heat island
Sustainable development goals

ABSTRACT

Understanding the seasonal variations in surface urban heat island (SUHI) in different local climate zones (LCZs) is crucial to efforts to reduce the impacts of urban warming on local residents. However, such an understanding is constrained by the lack of land surface temperatures (LSTs) at both high spatial and temporal resolutions. This study created time series LSTs by fusing Landsat 8 satellite data and gap-filled MODIS products to further analyses of the SUHI seasonality in a semi-arid city, Xi'an, China. The results showed that LSTs of the open building types were generally lower than those of the compact building types. The highest SUHI intensity (7.17 °C) was found in 'compact mid-rise buildings' (LCZ2), whereas lowest (3.62 °C) was found in 'open high-rise buildings' (LCZ4) in July. The SUHI intensity peaked about 17–23 days later than the background LST. The annual SUHI hysteresis cycles exhibited an anti-clockwise concave-up pattern in the monsoon-influenced hot-summer humid continental climate (Dwa per Köppen-Geiger climate scheme). The SUHI intensity in autumn was higher than in spring under the same background LST. These results provide valuable information for developing heat mitigation strategies in different seasons.

1. Introduction

Urbanization transforms natural ecosystems into systems in which humans and nature are linked together, which inevitably changes the thermal environment in urban areas. As a well-documented consequence of urbanization (Oke, 1982), urban heat islands (UHIs) can affect water and air quality (Grimm et al., 2008), and increase energy consumption (Santamouris et al., 2015) and human health risks (Patz et al., 2005). Therefore, understanding the characteristics of UHIs can facilitate the design of mitigation plans for reducing the impacts of urban warming on local residents and environment, thereby contributing to the achievement of the Sustainable Development Goal 11, "Make cities and human settlements inclusive, safe, resilient, and sustainable" (United Nations, 2015).

For many decades, the magnitude of the UHI effect has been quantified by simply calculating the difference in on-site temperature

* Corresponding author at: Key Laboratory of Digital Earth Science, Aerospace Information Research Institute, Chinese Academy of Sciences, No.9 Dengzhuang South Road, Haidian District, Beijing 100094, China.
E-mail address: lull@radi.ac.cn (L. Lu).

https://doi.org/10.1016/j.uclim.2023.101455
Received 16 September 2022; Received in revised form 9 January 2023; Accepted 11 February 2023
Available online 21 February 2023

measurements or remotely sensed surface temperature between 'urban' and 'rural' areas. However, this simple urban-rural difference can not reflect local climate variations within cities. In 2012, Stewart and Oke (2012) proposed the local climate zone (LCZ) framework to establish the relationship between different land surface types and the corresponding UHIs based on standardized descriptions. Each local climate zone corresponds to an area with uniform surface cover types, identical structure and material, and where human activities carried out are alike. LCZ mapping methods can be divided into three types: manual sampling methods, geographic information system (GIS)-based classification methods and remote sensing classification methods (Quan and Bansal, 2021). The World Urban Database and Access Portal Tools (WUDAPT) is a database dedicated to developing detailed, open urban databases for major cities across the world (Bechtel et al., 2015). It adopted a classification method for mapping local climate zones with free and open data and software tools (Bechtel et al., 2019a). With the development and availability of high-resolution satellite sensors in recent years, LCZ maps with much finer spatial detail have been created in multiple cities (Kim et al., 2021; Liu and Shi, 2020). In addition, the application of multi-temporal high resolution remote sensing images showed great potential to improve the classification accuracy of LCZ maps. For example, the use of multi-seasonal Sentinel-2 images and a recurrent residual network obtained the overall classification accuracy about 7% higher than single-seasonal images for LCZ mapping (Qiu et al., 2019). The convolutional neural networks with inputs of multi-temporal Sentinel-2 satellite data at 10 m spatial resolution yielded an overall classification accuracy of 86.5% for mapping LCZ (Rosentreter et al., 2020).

The surface urban heat island (SUHI) seasonality has been demonstrated in numerous studies based on remotely sensed land surface temperature (LST) observations (Deilami et al., 2018; Fu and Weng, 2018) and further supported by numerical simulations (Manoli et al., 2020). The MODIS LST was an extensively used dataset for examining the seasonality of SUHI intensity from local to global scales (Botje et al., 2022; Chakraborty and Lee, 2019; Dewan et al., 2021b; Eleftheriou et al., 2018; Wang et al., 2022). Since the coarse resolution MODIS data tends to underestimate SUHI intensity using LCZ scheme, remotely sensed thermal images with high spatial resolution was considered to be more suitable for thermal effect analysis of different LCZ types (Chen et al., 2020; Geletič et al., 2019; Xia et al., 2022). The seasonal nature of LST differences among various LCZs has been examined using Landsat LSTs in cities such as Szeged, Hungary (Gémes et al., 2016), English Bazar, India (Ziaul and Pal, 2018), and Shenyang, China (Zhao et al., 2021). Using cloud- and snow-free Landsat 8 data, Geletič et al. (2019) reported that the thermal behavior of urban local climates zones exhibited significant seasonal, diurnal and nocturnal differences in three central European cities. Previous studies also revealed that the SUHI presented a cyclic pattern over seasons, and such a pattern was mainly controlled by the time lags between the surface energy budget of cities and the energy/water fluxes in rural areas (Manoli et al., 2020). By quantifying the intensity of the SUHI in spring and fall for

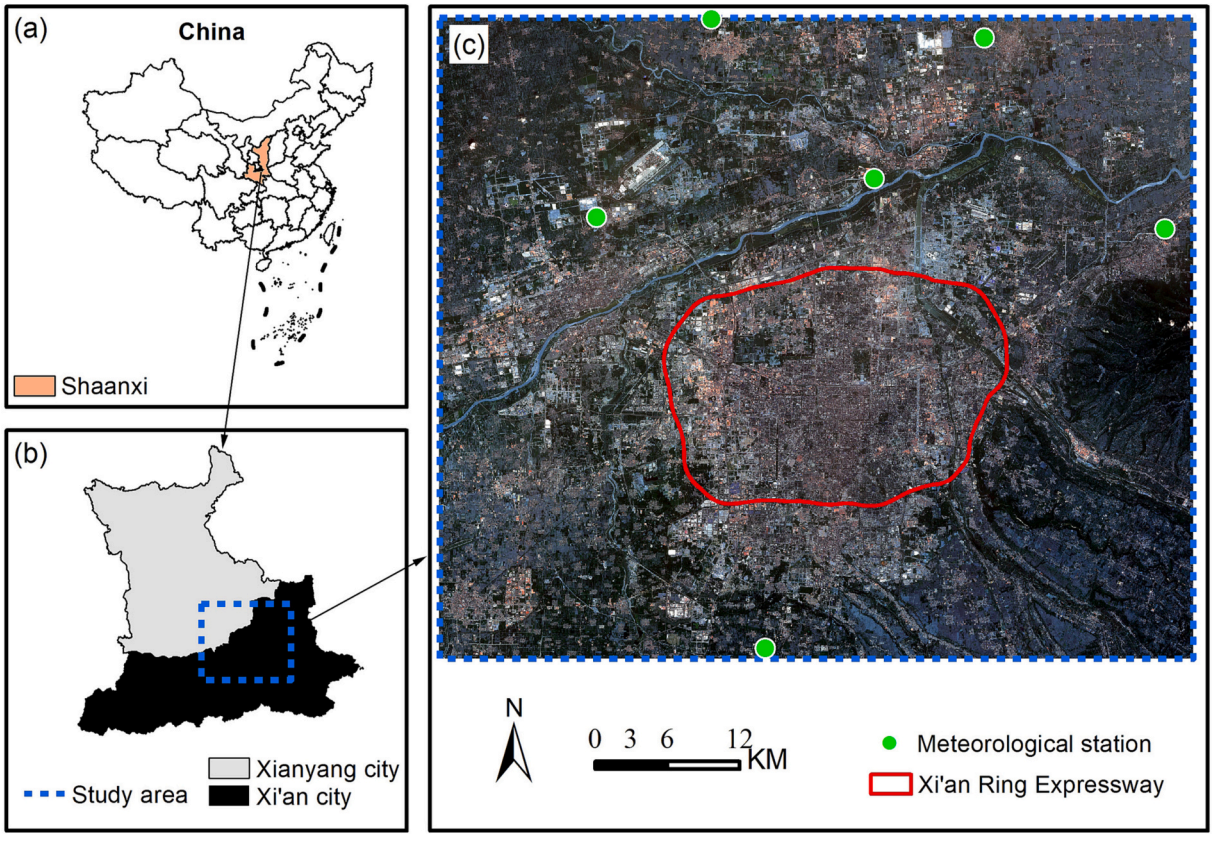

Fig. 1. Geographic location of the study area. (a) The location of Xi'an in China. (b) The spatial extent of the study area. (c) Meteorological stations in the study area. The underlying image is a true colour composite of Gaofen-1 acquired on July 2, 2020.

>130,000 city clusters in Europe, Zhou et al. (2013) revealed distinctive hysteretic patterns in the seasonality of SUHIs. Based on the MODIS daily LST product, Sismanidis et al. (2022) found that the seasonal hysteresis of the SUHIs differed across Köppen–Geiger climate classes. Their study also showed that the SUHI hysteresis was universally concave-up in wet climates, while more complex patterns were captured in dry climates. Since the SUHI hysteresis cycles differ considerably among cities in dry climates, further analysis can help enrich our knowledge of the SUHI seasonal characteristics in these areas.

Due to the lack of time series of high resolution land surface temperature data, remotely sensed LST images acquired on typical days have been used to characterize the SUHI for different months or seasons to explore the seasonal thermal behavior of LCZs (Geletič et al., 2019). This has led to large uncertainties in the analysis of temporal variations in urban thermal environment (Fu and Weng, 2016; Hu et al., 2020). The use of time series thermal remote sensing data to capture the seasonal changes of SUHI can remove some biases possibly introduced by the limited remote sensing scenes (Xian et al., 2022). Spatiotemporal data fusion methods provide a possible means of improving the resolution of remotely sensed LST data that will allow enhanced analysis of SUHIs (Gao et al., 2006). In particular, the enhanced spatial and temporal adaptive reflectance fusion model (ESTARFM) increases the accuracy of predicted fine-resolution remote sensing data, especially in the case of heterogeneous landscapes, and allows spatial detail to be preserved (Zhu et al., 2010). Compared with in-situ measurements, the ESTARFM was recognized as a practical data fusion method for LST data blending on clear days (Long et al., 2020). The implementation of gap-filling approaches further facilitated the generation of LST time series by making use of partly cloud-covered images (Knauer et al., 2016; Liu et al., 2020).

Since 2000, Xi'an has grown in size significantly and become a mega city in the semi-arid region in the northwestern China. Several studies have investigated the intensifying urban heat island effect in the city (Bechtel et al., 2019b; Lu et al., 2020), and these efforts mainly focused on the inter-annual variation in urban thermal environment (Han et al., 2022; Liu et al., 2019). Although understanding SUHI seasonality is crucial for the development of cooling strategies in water-scarce regions, a comprehensive investigation of the seasonal variations of SUHI in Xi'an was still needed. To address these gaps, this study aims to examine the seasonality and hysteresis cycles of the SUHI intensity in Xi'an by using the local climate zone framework and enhanced land surface temperature data. The LCZs were mapped using a random forest classifier and bi-seasonal high-resolution Gaofen-6 satellite images. Time series LSTs in 2020 were retrieved by fusing MODIS and Landsat data. The seasonal variability and hysteretic patterns of SUHIs in different LCZs were analyzed using statistical analysis and curve fitting.

2. Materials

2.1. Study area

Xi'an is a large inland city in the northwestern China (Fig. 1). According to the Köppen-Geiger climate zones (Beck et al., 2018), the majority of the study area belongs to the cold semi-arid climate (BSk), and a small part belongs to the monsoon-influenced humid subtropical climate (Cwa) and the monsoon-influenced hot-summer humid continental climate (Dwa). Winters are cold and dry; summers are hot and rainy. July has the highest average temperature. The study area included most parts of Xi'an along with the neighboring city of Xianyang and covered an area of about 3334.18 km^2. As a result of rapid urban development, a large amount of previously cultivated lands has been converted to built-up, and this has exacerbated the local UHI effect (Xu et al., 2020).

2.2. Datasets

The data sources used for the LCZ mapping included two Gaofen-6(GF-6) scenes, impervious surface data, and building footprint data. Details of these datasets are shown in Table 1.

Landsat, MODIS surface reflectance, and MODIS LST data were used as key inputs for the data fusion algorithm. The daily MOD09GA surface reflectance products (Vermote and Wolfe, 2015) containing red and near-infrared bands were obtained together with daily MOD11A1 LST data (Wan, 2014). The 8-day MODIS surface reflectance data (MOD09A1) (Vermote, 2015) and LST data (MOD11A2) (Wan et al., 2015) were also acquired. The MODIS products were downloaded from NASA's Land Processes Distributed Archive Center. Altogether, 4 Landsat and 100 MODIS image scenes were used (Table S1). The MODIS data products were re-projected to the geographic coordinate system of Landsat imagery and resampled to the spatial resolution of 30 m. Using the quality control layers from the MODIS LST products, clear sky pixels were selected for LST data fusion (Dewan et al., 2021a; Raj et al., 2020).

3. Method

The data processing required for the SUHI analysis consisted of several steps in this study (Fig. 2). First, a local climate zone map

Table 1
Datasets used for the LCZ classification.

Data type	Acquisition time	Source	Spatial resolution
GF-6	July 2, 2020	Chinese Academy of Sciences	Panchromatic 2 m; multispectral 8 m
GF-6	November 2, 2020	Chinese Academy of Sciences	Panchromatic 2 m; multispectral 8 m
Building footprint data	2020	Baidu Maps	Vector data
Impervious surface data	2020	Tsinghua University	30 m

was produced for the study area. The missing MODIS LST values were filled in, and the ESTARFM algorithm was used to generate the red, NIR and TIR bands of Landsat-like images. Based on fused data, time series of Landsat-like LSTs were retrieved. Finally, the differences in LST between the LCZ types and the seasonality in the SUHI intensity were analyzed.

3.1. Local climate zone classification

The GF-6 satellite imagery was first preprocessed – this consisted of radiometric calibration, ortho-rectification, project conversion, resampling, and image fusion. NDVI values were also calculated using the original GF-6 data acquired on July 2, 2020. Then, typical areas for each LCZ type were delineated using polygons as training samples. The training samples were vectorized using Google Earth by interpreters based on Google Earth, Street View maps and field observations. Finally, the preprocessed remote sensing data, vector data, and selected training areas were loaded into a random forest classifier to generate the local climate zone map of the study area.

3.2. Generation of Landsat-like land surface temperature data

Since data gaps exist in MOD11A2 LST images acquired on several dates, a model that recovered the missing data based on known pixel values from the same scene was constructed for each missing pixel. The predictors were the known values of pixels that had been selected based on quality flags. The relationships between known and missing pixels can be approximated based on historical data and using machine learning methods. For most of these algorithms, several hundred images are used to train the model, which can be described as:

$$D_{ijt} = F(T_{11k}, T_{21k}, T_{12K}, T_{22k}, \ldots, T_{nmk}) \quad (1)$$

where D_{ijt} is the temperature of the cloudy pixel in the ith row and jth column and t is the image acquisition time. T_{ijt} is the temperature of a known pixel located in row i and column j; $t = k$ indicates that information from the same image is used to estimate the value in the gap, and F is a function that can be estimated using machine learning algorithms (Sarafanov et al., 2020).

Support vector regression function was used to model the relationship between known and missing pixels in our study, and MOD11A2 LST images acquired between 2019 and 2021 as the historical images to fill the gaps. A gap filling example is illustrated in Fig. 3. The gap-filled MODIS LSTs were converted to TIR radiance at the effective wavelength of Landsat 8 band 10 using Planck's law.

The ESTARFM algorithm was used to generate Landsat-like data at 8-day temporal resolution. First, two fine-resolution Landsat images are used to find pixels that have values similar to the central pixel of a search window. Then, the weights of all the similar pixels

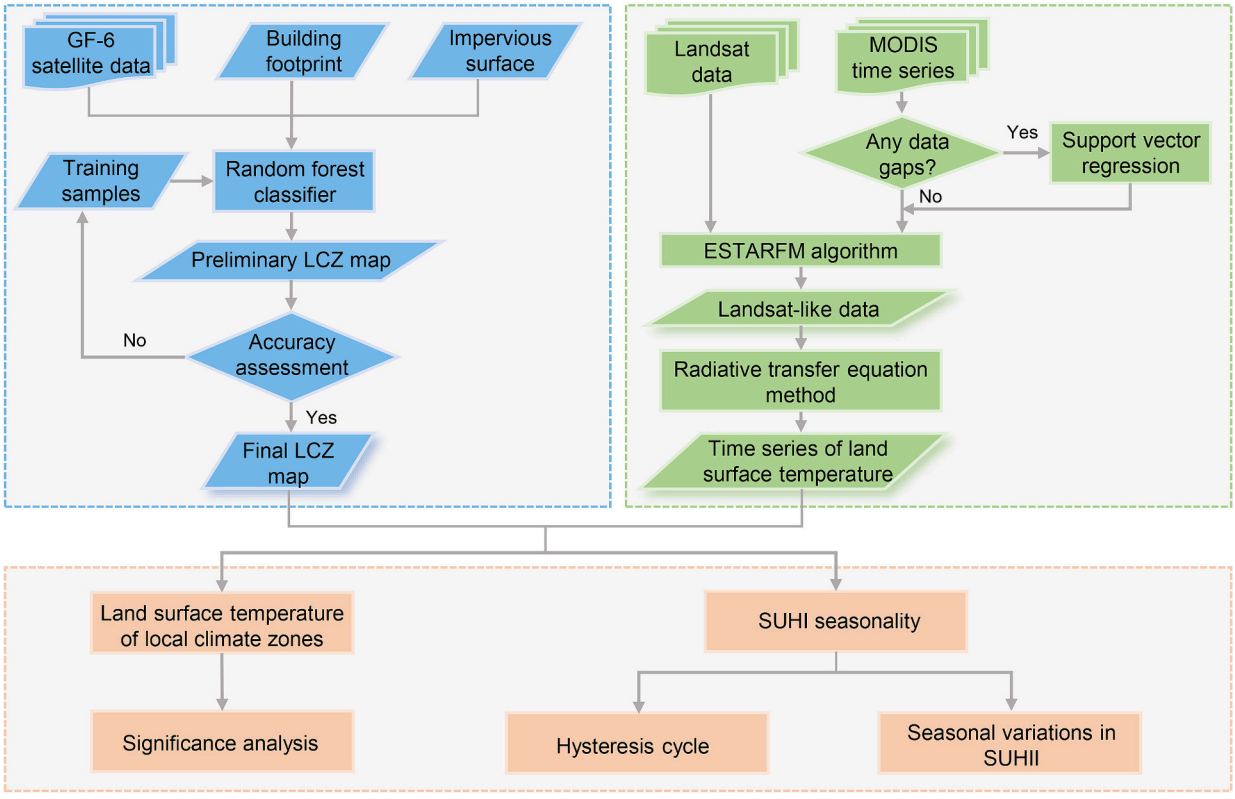

Fig. 2. Data processing workflow used in this study.

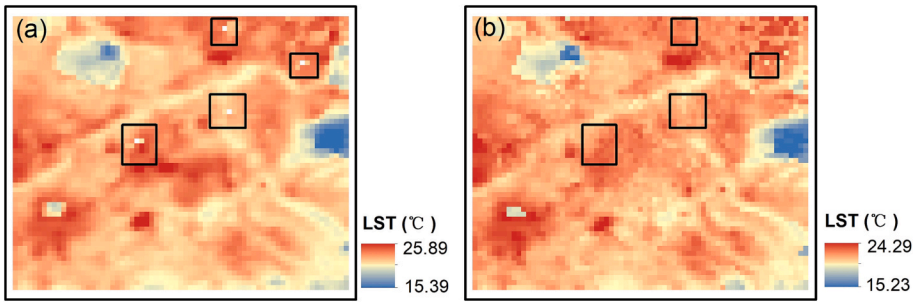

Fig. 3. An example of MODIS LST gap filling: (a) MODIS LST data from October 15, 2020 with missing values and (b) the same data after gap filling using the support vector regression method.

which represents the contribution of these pixels to the predicted change at the central pixel are calculated. Third, the conversion coefficient for the similar pixels within the coarse pixel is calculated using a linear regression model. Finally, the reflectance of the central pixel is obtained by combing the two predicted fine-resolution values.

The ESTARFM algorithm was performed on red, near infrared and TIR bands of the MODIS data, respectively. Three pairs of could-free Landsat and MODIS images were used as the start and end image pairs of the ESTARFM algorithm. The 8-day MODIS surface reflectance and LST images from dates between the start and end image pairs were used to predict Landsat-like images at corresponding dates. Using the Landsat-like data, a radiative transfer model was then used to retrieve the LSTs (Chatterjee et al., 2017). The thermal infrared radiance can be expressed as:

$$L_\lambda = B_\lambda(T_s)\varepsilon_\lambda\tau_{0\lambda} + L_{0\lambda}^{\uparrow} + (1-\varepsilon_\lambda)L_{0\lambda}^{\downarrow}\tau_{0\lambda} \tag{2}$$

where L_λ is the thermal infrared radiance at wavelength λ; $B_\lambda(T_s)$ represents the Planck blackbody brightness temperature for a physical surface temperature of T_s; ε_λ is the emissivity at wavelength λ; $\tau_{0\lambda}$ is the atmospheric transmission from the ground to the sensor; $L_{0\lambda}^{\uparrow}$ is the atmospheric upwelling radiation and $L_{0\lambda}^{\downarrow}$ is the atmospheric downwelling radiation.

According to Eq. (2), $B_\lambda(T_s)$ can be obtained as:

$$B_\lambda(T_s) = \frac{L_\lambda - L_{0\lambda}^{\uparrow} - \tau_{0\lambda}(1-\varepsilon_\lambda)L_{0\lambda}^{\downarrow}}{\varepsilon_\lambda\tau_{0\lambda}} \tag{3}$$

The emissivity is calculated using NDVI. The brightness temperature can then be converted to the land surface temperature, T_s, using the following equation:

$$T_s = \frac{K_2}{ln\left(1+\frac{k_1}{B_\lambda(T_s)}\right)} - 273.15 \tag{4}$$

The units of T_s in this equation are Celsius degrees; K_1 and K_2 are constants.

3.3. Surface heat island intensity calculation

The surface heat island intensity (SUHII) can be calculated as the difference between the average temperature of different built LCZ types and that of low-vegetation LCZ (LCZD) (Stewart and Oke, 2012). In this study, the SUHII was calculated using the following equation:

$$SUHII_{LCZX} = \overline{LST_{LCZX}} - \overline{LST_{LCZD}} \tag{5}$$

where $SUHII_{LCZX}$ represents the urban heat island intensity of LCZX, $\overline{LST_{LCZX}}$ represents the average surface temperature of LCZX and $\overline{LST_{LCZD}}$ represents the average surface temperature of the LCZD.

3.4. Statistical analysis

Kolmogorov–Smirnov normality tests (K—S tests) were performed to test the assumption that the land surface temperature data in the LCZs had a normal distribution (Geletič et al., 2019; Koc et al., 2018). The K—S test results showed that the LST data in each scene had a normal distribution at the 0.05 significance level. One-way ANOVA tests were then used to test the significance of the differences in LST between LCZ types. Since the LST data could not pass the homogeneity of variance test, Tamhane's T2 test was used as a post-hoc comparison method to determine which pairs of LCZs had significant differences (Kayri, 2009). The changes of SUHII characterized by LCZ2 (built LCZ with the maximum SUHII) and LCZ3 (built LCZ with the largest area) was plotted against the background temperature or the surface temperature of LCZD to analyze the annual cycle of SUHI. The seasonal hysteresis of SUHI was approximated by piecewise second-order polynomial functions.

4. Results

4.1. Local climate zone classification

A total of 16 LCZ types were recognized in the classified LCZ map (Fig. 4). The buildings outside the Xi'an Ring Expressway mainly belong to LCZ3 (compact low-rise). There are areas of dense forest (LCZA) and sparse forest (LCZB) in the east of the city. The LCZ types in the urban core mainly consist of LCZ1 and LCZ4 with other built LCZ types scattered throughout. Areas of vegetation are scattered throughout the urban core; this includes some large areas of vegetation, mainly in public parks. Water bodies account for 1.09% of the study area, and one major river – the Wei River – traverses the area. Woodland accounts for 12.03% of the study area, arable land 42.00% and the built-up area 42.66%.

Validation samples for various LCZ types were selected using high-resolution satellite imagery in Google Earth; at least 50 samples were selected for each LCZ type. The confusion matrix table can be found in Table S1. The overall classification accuracy is 92.99%, and the kappa coefficient is 0.91. The confusion matrix indicates that LCZ types with similar structures are prone to misclassification. In areas where the urban road network is not dense, LCZE (bare rock or paved cover) was misclassified as LCZ8 (large low-rise buildings).

4.2. Land surface temperature retrieval

Surface temperatures were measured hourly by in-situ instruments at the meteorological stations automatically (Fig. 1). The stations were set up in large and flat areas with homogenous surface covers. The 0 cm surface temperature records closest to the overpass time of Landsat 8 satellite were compared with the LSTs retrieved from remote sensing data (Coll et al., 2010; Xia et al., 2022). The mean absolute difference (MAD), root mean square error (RMSE) and Pearson's correlation coefficient (Pearson's r) were used to evaluate the accuracy of the retrieved LSTs. The MAD and RMSE between the predicted and observed LSTs were 1.17 °C and 2.75 °C, respectively. The value of Pearson's r was 0.98 with a significance level of 0.01, indicating a strong correlation between the remotely sensed and observed LSTs (Fig. 5).

The LST data obtained from the Landsat image on April 9, 2020 was also used to evaluate the accuracy of the LST generated using the data fusion algorithm on the same date (Weng et al., 2014). At the significance level of 0.05, MAD and RMSE were 0.62 °C and 1.31 °C, respectively, and Pearson's r value was 0.84. These results indicated that there was a strong correlation between the predicted and observed LST (Fig. 6).

4.3. Surface urban heat island intensity differences between LCZs

The monthly variations in the SUHII of the different LCZ types were illustrated using a heat map (Fig. 7). The difference between the SUHII of the built types (especially LCZ1–LCZ5) and the natural types (LCZA–LCZD) is greater in June, July, and August than in the other months. Within the built LCZ types, the compact LCZs (LCZ1–LCZ3) with sparse vegetation exhibit a stronger heat island effect than the open LCZs (LCZ4–LCZ6) with dense green coverage. The high surface temperature of LCZ8 (large low-rise buildings) is related to the difficulty of dissipating heat from large buildings and the large amount of paving. LCZA (dense trees), one of the 'vegetation' LCZ

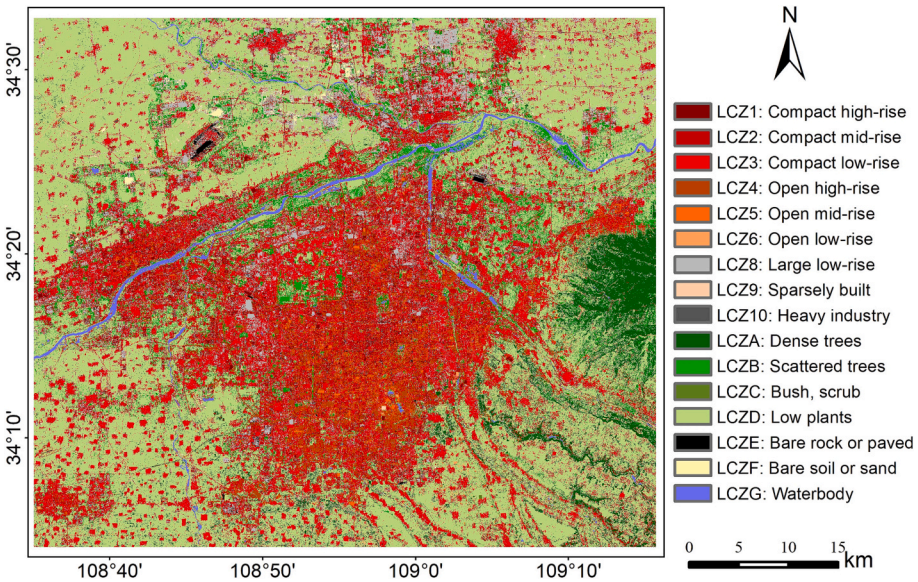

Fig. 4. Local climate zone map of Xi'an in 2020.

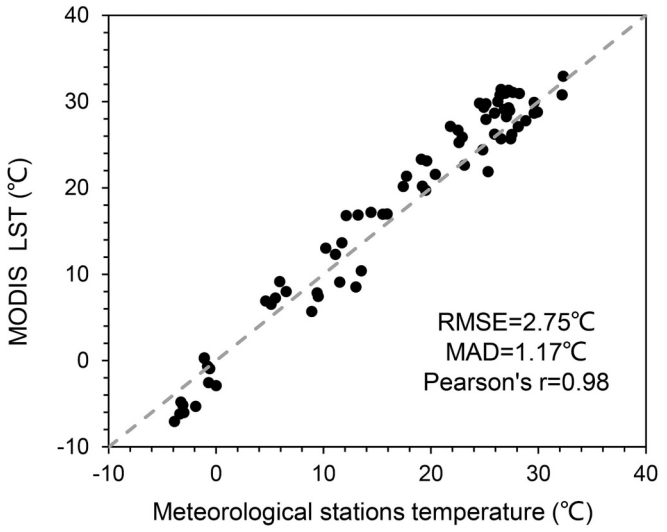

Fig. 5. Validation of the retrieved surface temperature data using in situ data collected from meteorological stations.

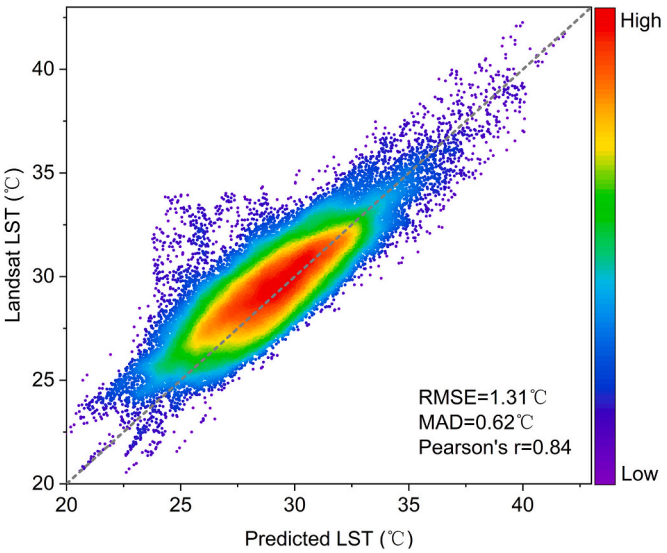

Fig. 6. The scatter plot between the estimated and the observed Landsat land surface temperature data.

	1	2	3	4	5	6	8	9	10	A	B	C	D	E	F	G
January	1.14	1.94	2.04	0.47	1.11	1.07	1.92	-0.46	1.83	-1.32	-0.25	-0.54	0.00	2.44	0.83	-4.39
February	-0.02	0.54	1.21	-0.89	-0.29	0.25	1.40	-0.49	0.97	-1.30	-0.52	-0.78	0.00	1.48	0.98	-4.75
March	1.40	2.38	2.06	0.82	1.52	1.16	1.98	0.40	2.06	-0.80	0.29	0.26	0.00	2.58	1.08	-4.15
April	2.34	3.21	2.60	1.27	1.99	1.50	2.84	0.28	3.19	-1.54	1.00	-0.92	0.00	3.45	1.87	-3.12
May	3.69	4.88	3.48	3.03	3.77	2.57	3.40	0.62	3.79	-1.43	1.31	-0.28	0.00	4.15	1.59	-2.28
June	4.18	6.27	4.19	3.47	4.76	3.17	3.92	-0.18	3.63	-2.35	0.22	-0.19	0.00	4.75	0.79	-6.02
July	5.25	7.17	4.54	3.62	5.84	4.88	4.04	0.84	4.67	-1.50	0.94	-0.04	0.00	5.21	0.82	-3.54
August	5.12	7.04	4.84	3.88	5.78	4.78	4.25	0.89	4.87	-1.64	1.19	0.08	0.00	5.61	1.04	-4.04
September	2.87	4.23	3.44	1.87	2.89	2.35	3.24	-0.02	3.32	-1.61	0.48	0.14	0.00	4.08	0.99	-4.69
October	1.56	2.49	2.38	0.79	1.52	1.44	2.39	-0.59	1.89	-1.64	-0.05	-0.25	0.00	2.71	0.77	-4.47
November	1.81	2.92	2.38	1.20	2.01	1.49	2.23	-0.11	2.16	-0.21	0.21	0.40	0.00	2.77	0.88	-3.55
December	0.40	1.39	1.48	-0.02	0.71	0.79	1.37	-0.33	0.63	-1.32	-0.95	-0.01	0.00	1.40	0.28	-4.74

High

Low

Fig. 7. Heat map of the SUHII for all LCZs in each month of 2020. Red indicates high intensity, and blue indicates low intensity. (For interpretation of the references to colour in this figure legend, the reader is referred to the web version of this article.)

types, has the lowest surface temperature, which indicates that there is a greater cooling effect associated with this LCZ than with LCZB, LCZC and LCZD. In all seasons, the LSTs of LCZE (bare rock or paved) and LCZF (bare soil or sand) are similar to those of the built LCZs.

The results of pairwise comparisons of the LST data for different groups of LCZs are shown in Fig. 8. The results of the one-way ANOVA indicated that there were significant differences between the mean LSTs of selected LCZs (0.05 significance level). Based on our analysis, 94.17% of the LCZ pairs exhibited a significant difference in winter(Fig. 8(d)). In the other three seasons (Fig. 8(a-c)), the proportion was 96.67%.

4.4. Seasonality of the surface urban heat island

The seasonal distribution of the SUHII shows large spatial variations in the study area (Fig. 9). Inside the inner ring highway, in areas to the north of this highway and along the Wei River, the SUHII begins to increase in spring. In summer, the SUHII is between 3 °C and 5 °C (except LCZ9) for the built LCZs, with the areas having the greatest SUHII (> 5 °C) being mostly downtown areas corresponding to LCZ2 (compact mid-rise) and LCZ5 (open mid-rise). The areas with a low SUHII (i.e., the areas in green in Fig. 9) consist mainly of rural areas outside the Ring Expressway and correspond to LCZA, LCZB and LCZD. Autumn appears to be a turning point in the SUHII patterns and that the SUHII decreases significantly from then onward. In winter, cold 'islands' appear in parts of the main urban area. The SUHII for LCZG (water body) and LCZA (dense forest), found in the east of the study area, is <0 °C throughout the year, and these areas thus provide a cooling effect in all seasons.

Based on the LCZ map and monthly LST data, the annual cycle of background LST represented by LST of LCZD and SUHI and resulted seasonal hysteresis were further investigated (Fig. 10). The phase shift between SUHI intensity and background temperature (Fig. 10(a)) demonstrates the existence of seasonal hysteresis (Zhou et al., 2013). The annual intensity of SUHI of LCZ2 and LCZ3 peaks 17 and 23 days later than the peak of background temperature, respectively. The diurnal SUHI hysteresis cycles (Fig. 10(b)) exhibited an anti-clockwise concave-up pattern. Given the same background temperature, higher values in SUHI occur in October and November compared to those in March and April.

5. Discussion

5.1. Land surface temperature differences between LCZs

The application of the WUDAPT method has previously achieved an OA of 52% for LCZ mapping in Xi'an (He et al., 2018). OAs higher than 80% have been reported for studies in Europe (Verdonck et al., 2017) and North America (Wang et al., 2018), where urban forms are generally more homogenous. The overall accuracy of the results obtained by this study is 92.99%, which outperforms most previous studies that used medium-resolution remote sensing data. To reduce confusion between different LCZ types, a vector building

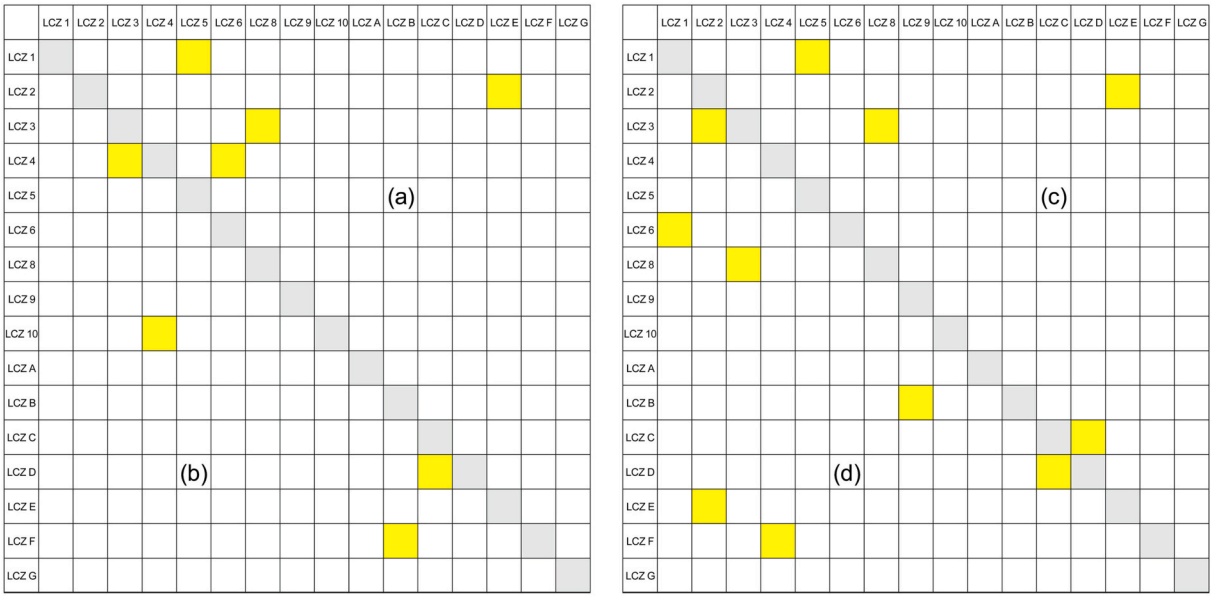

Fig. 8. Significance of the differences between the LSTs of LCZ pairs in each season calculated using Tamhane's T2 test for (a) spring, (b) summer, (c) autumn and (d) winter. A yellow cell indicates no significant difference between the LSTs of the LCZs(p-value>0.05). A blank cell represents significant difference between the LCZs (p-value≤0.05). (For interpretation of the references to colour in this figure legend, the reader is referred to the web version of this article.)

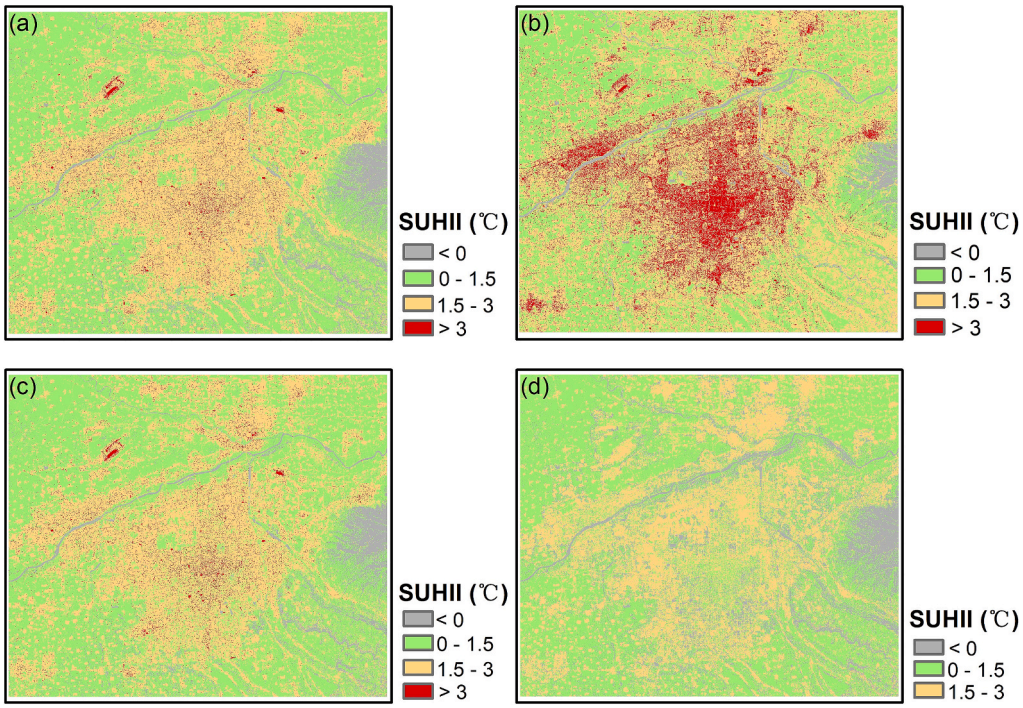

Fig. 9. Spatial distribution of the SUHII in the study area in (a) spring, (b) summer, (c) autumn and (d) winter.

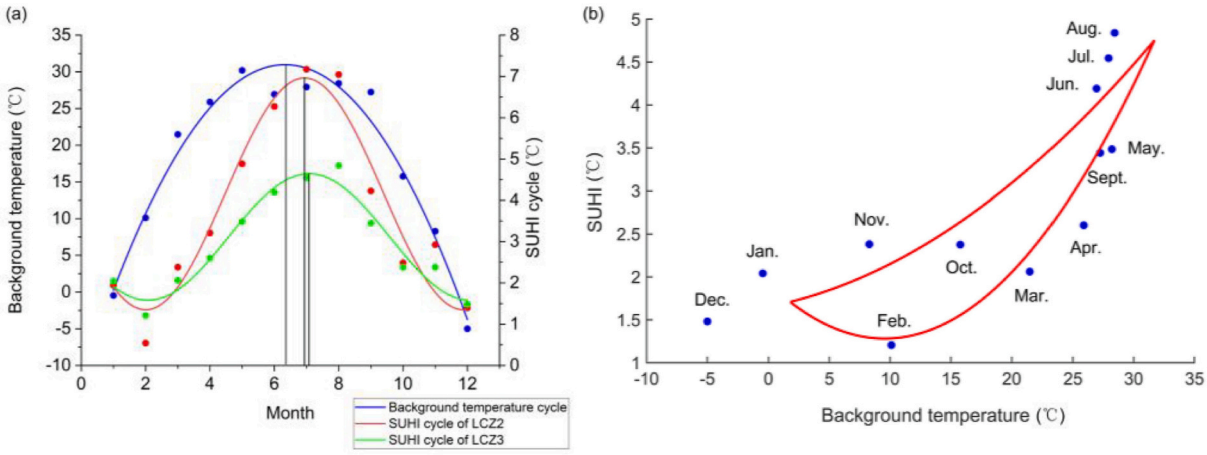

Fig. 10. Annual cycles of SUHII and background temperature (a) and resulting hysteretic curves (b) in the study area.

height map was also used. Due to the strong ability of capturing and learning contextual information, deep neural networks are very suitable to predict the highly context-based LCZs over a large area (Rosentreter et al., 2020; Yoo et al., 2019). Sophisticated network architectures have been developed to produce LCZ maps using Sentinel-2 data for Asian (Kim et al., 2021), European (Qiu et al., 2019) and global cities (Zhu et al., 2022). Deep learning methods can be tested to further optimize the LCZ map in future studies.

In this study, urban landscapes consisting of compact buildings (LCZ1–LCZ3), among which LCZ2 had the highest SUHII at 7.17 °C in July, generally had a greater heat island intensity than areas of open buildings (LCZ4–LCZ6). LCZs with high building densities have less space for ventilation and cooling and are associated with higher surface temperatures. Our results also indicate that the SUHII of LCZ4(open high-rise) is the lowest among the built LCZ types, because this LCZ type includes more green space than the low-rise building types and is well ventilated. Among the natural LCZs, LCZG had the lowest SUHII at −6.02 °C, which indicates that water bodies can effectively reduce the LST. Dense trees (LCZA) provide better cooling effects than sparse trees, shrubs and grasses.

5.2. Seasonality of the surface urban heat island

Although Zhou et al. (2013) reported that cities usually showed a concave down curve with peak SUHI in spring in dry regions in Europe, Sismanidis et al. (2022) found that the diurnal SUHII and rural LST for semi-arid cities was generally strongest in July/August. According to Sismanidis et al. (2022), the SUHII and rural LSTs of cities in the Dwa climate became maximum almost simultaneously in July/August, while the daytime SUHII of cities in the Cwa climate reached maximum in August/September. Our study demonstrate that the maximum of background temperature appeared in June, while the SUHI intensity peaked in July in the study area. The hysteresis cycles of diurnal SUHI in cities in the BSk climate varied with geographic location and could take the form of concave-down, flat, twisted, and triangle-like loops (Sismanidis et al., 2022). The anti-clockwise upward concave curve in this study agreed well with the average diurnal SUHII hysteresis loops in the Dwa continental climates captured using MODIS data (Sismanidis et al., 2022). Therefore, the seasonality of SUHI in the study area in the Dwa was mainly characterized.

5.3. Limitations and prospects

The fused remote sensing data with 30 m resolution was used to explore the seasonality of SUHI in the study area. The observed SUHI seasonality improved our knowledge on seasonal hysteresis of SUHI in a semi-arid city. However, the surface cover in urban areas is highly heterogeneous. Due to the limited spatial resolution of remote sensing data, the landscape components within a single pixel are usually complicated and mixed. This may lead to uncertainties in the evaluation results. Satellite or airborne remote sensing data with a higher spatial resolution can be obtained to capture more accurate SUHI variations (Koc et al., 2018). Secondly, the proposed methodologies should be applied to more cities to derive a more generalized insight on the hysteretic patterns of SUHI in dry climates (Lu et al., 2019). Finally, a comprehensive analysis of the impacts of natural and anthropogenic factors on SUHI may provide insights to develop effective thermal mitigation strategies in the study area.

6. Conclusions

Time series LSTs were generated by fusing Landsat 8 and MODIS data for each month of 2020. High-resolution GF-6 remote sensing images, impervious surface products and building footprint data were used to create a highly accurate LCZ map. Using the LCZ classification map and enhanced LST data, the seasonality of the SUHI in Xi'an, a mega city in semi-arid climate region, were investigated. The close correlation between the estimated and observed LSTs demonstrates the feasibility of using gap-filling and the ESTARFM algorithm to retrieve LSTs with a high spatial and temporal resolution. Among the built LCZs, the surface temperatures of the open building types were generally lower than those of the compact building types. LCZ2 was found to have the highest SUHII of 7.17 °C in summer; the SUHII of LCZ4 was lowest (3.62 °C). The maximum intensity of SUHI appears about 17–23 days later than the maximum background temperature, and the hysteresis cycles of SUHI exhibited an anti-clockwise concave-up pattern. The seasonal hysteresis of SUHI in the study area matched the urban climatology of cities in the Dwa climate. Compared with temporally discontinuous data, the enhance LSTs captured the variations of SUHI more accurately. These results provide useful information to urban planners for improving urban thermal environment and mitigating the negative effects of heat islands.

Fund

This work was supported by the Director Fund of the International Research Center of Big Data for Sustainable Development Goals (grant number CBAS2022DF016) and the National Natural Science Foundation of China (grant number 42071321).

CRediT authorship contribution statement

Liying Han: Methodology, Software, Validation, Formal analysis, Data curation, Writing – original draft, Visualization. **Linlin Lu:** Conceptualization, Methodology, Formal analysis, Investigation, Writing – review & editing, Supervision, Funding acquisition. **Peng Fu:** Formal analysis, Writing – review & editing. **Chao Ren:** Investigation, Writing – review & editing. **Meng Cai:** Validation, Data curation. **Qingting Li:** Resources, Project administration.

Declaration of Competing Interest

The authors declare that they have no known competing financial interests or personal relationships that could have appeared to influence the work reported in this paper.

Data availability

The remote sensing and geospatial datasets used in this study can be accessed upon request to the corresponding author.

Acknowledgments

The authors would like to thank the editors and anonymous reviewers for their constructive and helpful comments.

Appendix A. Supplementary data

Supplementary data to this article can be found online at https://doi.org/10.1016/j.uclim.2023.101455.

References

Bechtel, B., Alexander, P.J., Böhner, J., Ching, J., Conrad, O., Feddema, J., Mills, G., See, L., Stewart, I., 2015. Mapping local climate zones for a worldwide database of the form and function of cities. ISPRS Int. J. Geo Inf. 4, 199–219. https://doi.org/10.3390/ijgi4010199.

Bechtel, B., Alexander, P.J., Beck, C., Böhner, J., Brousse, O., Ching, J., Demuzere, M., Fonte, C., Gál, T., Hidalgo, J., Hoffmann, P., Middel, A., Mills, G., Ren, C., See, L., Sismanidis, P., Verdonck, M.-L., Xu, G., Xu, Y., 2019a. Generating WUDAPT level 0 data – current status of production and evaluation. Urban Clim. 27, 24–45. https://doi.org/10.1016/j.uclim.2018.10.001.

Bechtel, B., Demuzere, M., Mills, G., Zhan, W., Sismanidis, P., Small, C., Voogt, J., 2019b. SUHI analysis using local climate zones—a comparison of 50 cities. Urban Clim. 28, 100451 https://doi.org/10.1016/j.uclim.2019.01.005.

Beck, H.E., Zimmermann, N.E., McVicar, T.R., Vergopolan, N., Berg, A., Wood, E.F., 2018. Present and future Köppen-Geiger climate classification maps at 1-km resolution. Sci. Data 5, 180214. https://doi.org/10.1038/sdata.2018.214.

Botje, D., Dewan, A., Chakraborty, T.C., 2022. Comparing coarse-resolution land surface temperature products over western Australia. Remote Sens. 14 (10) https://doi.org/10.3390/rs14102296.

Chakraborty, T., Lee, X., 2019. A simplified urban-extent algorithm to characterize surface urban heat islands on a global scale and examine vegetation control on their spatiotemporal variability. Int. J. Appl. Earth Obs. Geoinf. 74, 269–280. https://doi.org/10.1016/j.jag.2018.09.015.

Chatterjee, R.S., Singh, N., Thapa, S., Sharma, D., Kumar, D., 2017. Retrieval of land surface temperature (LST) from landsat TM6 and TIRS data by single channel radiative transfer algorithm using satellite and ground-based inputs. Int. J. Appl. Earth Obs. Geoinf. 58, 264–277. https://doi.org/10.1016/j.jag.2017.02.017.

Chen, X., Xu, Y., Yang, J., Wu, Z., Zhu, H., 2020. Remote sensing of urban thermal environments within local climate zones: a case study of two high-density subtropical Chinese cities. Urban Clim. 31, 100568 https://doi.org/10.1016/j.uclim.2019.100568.

Coll, C., Galve, J.M., Sanchez, J.M., Caselles, V., 2010. Validation of Landsat-7/ETM+ thermal-band calibration and atmospheric correction with ground-based measurements. IEEE Trans. Geosci. Remote Sens. 48, 547–555. https://doi.org/10.1109/TGRS.2009.2024934.

Deilami, K., Kamruzzaman, M., Liu, Y., 2018. Urban heat island effect: a systematic review of spatio-temporal factors, data, methods, and mitigation measures. Int. J. Appl. Earth Obs. Geoinf. 67, 30–42. https://doi.org/10.1016/j.jag.2017.12.009.

Dewan, A., Kiselev, G., Botje, D., 2021a. Diurnal and seasonal trends and associated determinants of surface urban heat islands in large Bangladesh cities. Appl. Geogr. 135, 102533 https://doi.org/10.1016/j.apgeog.2021.102533.

Dewan, A., Kiselev, G., Botje, D., Mahmud, G.I., Bhuian, M.H., Hassan, Q.K., 2021b. Surface urban heat island intensity in five major cities of Bangladesh: patterns, drivers and trends. Sustain. Cities Soc. 71, 102926 https://doi.org/10.1016/j.scs.2021.102926.

Eleftheriou, D., Kiachidis, K., Kalmintzis, G., Kalea, A., Bantasis, C., Koumadoraki, P., Gemitzi, A., 2018. Determination of annual and seasonal daytime and nighttime trends of MODIS LST over Greece - climate change implications. Sci. Total Environ. 616-617, 937–947. https://doi.org/10.1016/j.scitotenv.2017.10.226.

Fu, P., Weng, Q., 2016. A time series analysis of urbanization induced land use and land cover change and its impact on land surface temperature with Landsat imagery. Remote Sens. Environ. 175, 205–214. https://doi.org/10.1016/j.rse.2015.12.040.

Fu, P., Weng, Q., 2018. Variability in annual temperature cycle in the urban areas of the United States as revealed by MODIS imagery. ISPRS J. Photogramm. Remote Sens. 146, 65–73. https://doi.org/10.1016/j.isprsjprs.2018.09.003.

Gao, F., Masek, J., Schwaller, M., Hall, F., 2006. On the blending of the Landsat and MODIS surface reflectance: predicting daily Landsat surface reflectance. IEEE Trans. Geosci. Remote Sens. 44, 2207–2218. https://doi.org/10.1109/TGRS.2006.872081.

Geletič, J., Lehnert, M., Savić, S., Milošević, D., 2019. Inter−/intra-zonal seasonal variability of the surface urban heat island based on local climate zones in three central European cities. Build. Environ. 156, 21–32. https://doi.org/10.1016/j.buildenv.2019.04.011.

Gémes, O., Tobak, Z., van Leeuwen, B., 2016. Satellite based analysis of surface urban heat island intensity. J. Environ. Geogr. 9, 23–30. https://doi.org/10.1515/jengeo-2016-0004.

Grimm, N.B., Faeth, S.H., Golubiewski, N.E., Redman, C.L., Wu, J., Bai, X., Briggs, J.M., 2008. Global change and the ecology of cities. Science 319, 756–760. https://doi.org/10.1126/science.1150195.

Han, B., Luo, Z., Liu, Y., Zhang, T., Yang, L., 2022. Using local climate zones to investigate spatio-temporal evolution of thermal environment at the urban regional level: a case study in Xi'an, China. Sustain. Cities Soc. 76, 103495 https://doi.org/10.1016/j.scs.2021.103495.

He, S., Zhang, Y., Gu, Z., Su, J., 2018. Local climate zone classification with different source data in Xi'an, China. Indoor Built Environ. 28, 1190–1199. https://doi.org/10.1177/1420326X18796545.

Hu, L., Sun, Y., Collins, G., Fu, P., 2020. Improved estimates of monthly land surface temperature from MODIS using a diurnal temperature cycle (DTC) model. ISPRS J. Photogramm. Remote Sens. 168, 131–140. https://doi.org/10.1016/j.isprsjprs.2020.08.007.

Kayri, M., 2009. The multiple comparison (post-hoc) techniques to determine the difference between groups in researches. Fırat Univ. J. Soc. Sci. 19, 51–64.

Kim, M., Jeong, D., Kim, Y., 2021. Local climate zone classification using a multi-scale, multi-level attention network. ISPRS J. Photogramm. Remote Sens. 181, 345–366. https://doi.org/10.1016/j.isprsjprs.2021.09.015.

Knauer, K., Gessner, U., Fensholt, R., Kuenzer, C., 2016. An ESTARFM fusion framework for the generation of large-scale time series in cloud-prone and heterogeneous landscapes. Remote Sens. 8 (5), 425. https://doi.org/10.3390/rs8050425.

Koc, C.B., Osmond, P., Peters, A., Irger, M., 2018. Understanding land surface temperature differences of local climate zones based on airborne remote sensing data. IEEE J. Sel. Top. Appl. Earth Obs. Remote Sens. 11, 2724–2730. https://doi.org/10.1109/JSTARS.2018.2815004.

Liu, S., Shi, Q., 2020. Local climate zone mapping as remote sensing scene classification using deep learning: a case study of metropolitan China. ISPRS J. Photogramm. Remote Sens. 164, 229–242. https://doi.org/10.1016/j.isprsjprs.2020.04.008.

Liu, S., Zang, Z., Wang, W., Wu, Y., 2019. Spatial-temporal evolution of urban heat island in Xi'an from 2006 to 2016. Phys. Chem. Earth Parts A/B/C 110, 185–194. https://doi.org/10.1016/j.pce.2018.11.007.

Liu, X., Zhou, Y., Yue, W., Li, X., Liu, Y., Lu, D., 2020. Spatiotemporal patterns of summer urban heat island in Beijing, China using an improved land surface temperature. J. Clean. Prod. 257, 120529 https://doi.org/10.1016/j.jclepro.2020.120529.

Long, D., Yan, L., Bai, L., Zhang, C., Li, X., Lei, H., Yang, H., Tian, F., Zeng, C., Meng, X., Shi, C., 2020. Generation of MODIS-like land surface temperatures under all-weather conditions based on a data fusion approach. Remote Sens. Environ. 246, 111863 https://doi.org/10.1016/j.rse.2020.111863.

Lu, L., Weng, Q., Guo, H., Feng, S., Li, Q., 2019. Assessment of urban environmental change using multi-source remote sensing time series (2000–2016): a comparative analysis in selected megacities in Eurasia. Sci. Total Environ. 684, 567–577. https://doi.org/10.1016/j.scitotenv.2019.05.344.

Lu, L., Weng, Q., Xiao, D., Guo, H., Li, Q., Hui, W., 2020. Spatiotemporal variation of surface urban heat islands in relation to land cover composition and configuration: a multi-scale case study of Xi'an, China. Remote Sens. 12, 2713. https://doi.org/10.3390/rs12172713.

Manoli, G., Fatichi, S., Bou-Zeid, E., Katul, G.G., 2020. Seasonal hysteresis of surface urban heat islands. Proc. Natl. Acad. Sci. 117, 7082–7089. https://doi.org/10.1073/pnas.1917554117.

Oke, T.R., 1982. The energetic basis of the urban heat island. Q. J. R. Meteorol. Soc. 108, 1–24. https://doi.org/10.1002/qj.49710845502.

Patz, J.A., Campbell-Lendrum, D., Holloway, T., Foley, J.A., 2005. Impact of regional climate change on human health. Nature 438, 310–317. https://doi.org/10.1038/nature04188.

Qiu, C., Mou, L., Schmitt, M., Zhu, X.X., 2019. Local climate zone-based urban land cover classification from multi-seasonal Sentinel-2 images with a recurrent residual network. ISPRS J. Photogramm. Remote Sens. 154, 151–162. https://doi.org/10.1016/j.isprsjprs.2019.05.004.
Quan, S.J., Bansal, P., 2021. A systematic review of GIS-based local climate zone mapping studies. Build. Environ. 196, 107791 https://doi.org/10.1016/j.buildenv.2021.107791.
Raj, S., Paul, S.K., Chakraborty, A., Kuttippurath, J., 2020. Anthropogenic forcing exacerbating the urban heat islands in India. J. Environ. Manag. 257, 110006 https://doi.org/10.1016/j.jenvman.2019.110006.
Rosentreter, J., Hagensieker, R., Waske, B., 2020. Towards large-scale mapping of local climate zones using multitemporal sentinel 2 data and convolutional neural networks. Remote Sens. Environ. 237, 111472 https://doi.org/10.1016/j.rse.2019.111472.
Santamouris, M., Cartalis, C., Synnefa, A., Kolokotsa, D., 2015. On the impact of urban heat island and global warming on the power demand and electricity consumption of buildings—a review. Energy Build. 98, 119–124. https://doi.org/10.1016/j.enbuild.2014.09.052.
Sarafanov, M., Kazakov, E., Nikitin, N.O., Kalyuzhnaya, A.V., 2020. A machine learning approach for remote sensing data gap-filling with open-source implementation: an example regarding land surface temperature, surface albedo and NDVI. Remote Sens. 12, 3865. https://doi.org/10.3390/rs12233865.
Sismanidis, P., Bechtel, B., Perry, M., Ghent, D., 2022. The seasonality of surface urban heat islands across climates. Remote Sens. 14, 2318. https://doi.org/10.3390/rs14102318.
Stewart, I.D., Oke, T.R., 2012. Local climate zones for urban temperature studies. Bull. Am. Meteorol. Soc. 93, 1879–1900. https://doi.org/10.1175/BAMS-D-11-00019.1.
United Nations, 2015. Transforming our world: the 2030 Agenda for Sustainable Development. Available online: http://www.un.org/ga/search/view_doc.asp?symbol=A/RES/.70/1&Lang=E (accessed on 30 June 2022).
Verdonck, M.-L., Okujeni, A., van der Linden, S., Demuzere, M., De Wulf, R., Van Coillie, F., 2017. Influence of neighbourhood information on 'local climate zone' mapping in heterogeneous cities. Int. J. Appl. Earth Obs. Geoinf. 62, 102–113. https://doi.org/10.1016/j.jag.2017.05.017.
Vermote, E., 2015. MOD09A1 MODIS/Terra Surface Reflectance 8-Day L3 Global 500m SIN Grid V006. NASA EOSDIS Land Processes DAAC. https://doi.org/10.5067/MODIS/MOD09A1.006.
Vermote, E., Wolfe, R., 2015. MOD09GA MODIS/Terra Surface Reflectance Daily L2G Global 1kmand 500m SIN Grid V006. NASA EOSDIS Land Processes DAAC. https://doi.org/10.5067/MODIS/MOD09GA.006.
Wan, Z., 2014. New refinements and validation of the collection-6 MODIS land-surface temperature/emissivity product. Remote Sens. Environ. 140, 36–45. https://doi.org/10.1016/j.rse.2013.08.027.
Wan, Z., Hook, S., Hulley, G., 2015. MOD11A2 MODIS/Terra Land Surface Temperature/Emissivity 8-Day L3 Global 1km SIN Grid V006. NASA EOSDIS Land Processes DAAC. https://doi.org/10.5067/MODIS/MOD11A2.006.
Wang, C., Middel, A., Myint, S.W., Kaplan, S., Brazel, A.J., Lukasczyk, J., 2018. Assessing local climate zones in arid cities: the case of Phoenix, Arizona and Las Vegas, Nevada. ISPRS J. Photogramm. Remote Sens. 141, 59–71. https://doi.org/10.1016/j.isprsjprs.2018.04.009.
Wang, Y.-R., Hessen, D.O., Samset, B.H., Stordal, F., 2022. Evaluating global and regional land warming trends in the past decades with both MODIS and ERA5-land land surface temperature data. Remote Sens. Environ. 280, 113181 https://doi.org/10.1016/j.rse.2022.113181.
Weng, Q., Fu, P., Gao, F., 2014. Generating daily land surface temperature at Landsat resolution by fusing Landsat and MODIS data. Remote Sens. Environ. 145, 55–67. https://doi.org/10.1016/j.rse.2014.02.003.
Xia, H., Chen, Y., Song, C., Li, J., Quan, J., Zhou, G., 2022. Analysis of surface urban heat islands based on local climate zones via spatiotemporally enhanced land surface temperature. Remote Sens. Environ. 273, 112972 https://doi.org/10.1016/j.rse.2022.112972.
Xian, G., Shi, H., Zhou, Q., Auch, R., Gallo, K., Wu, Z., Kolian, M., 2022. Monitoring and characterizing multi-decadal variations of urban thermal condition using time-series thermal remote sensing and dynamic land cover data. Remote Sens. Environ. 269, 112803 https://doi.org/10.1016/j.rse.2021.112803.
Xu, D., Zhou, D., Wang, Y., Meng, X., Chen, W., Yang, Y., 2020. Temporal and spatial variations of urban climate and derivation of an urban climate map for Xi'an, China. Sustain. Cities Soc. 52, 101850 https://doi.org/10.1016/j.scs.2019.101850.
Yoo, C., Han, D., Im, J., Bechtel, B., 2019. Comparison between convolutional neural networks and random forest for local climate zone classification in mega urban areas using Landsat images. ISPRS J. Photogramm. Remote Sens. 157, 155–170. https://doi.org/10.1016/j.isprsjprs.2019.09.009.
Zhao, Z., Sharifi, A., Dong, X., Shen, L., He, B.-J., 2021. Spatial variability and temporal heterogeneity of surface urban heat island patterns and the suitability of local climate zones for land surface temperature characterization. Remote Sens. 13 (21), 4338. https://doi.org/10.3390/rs13214338.
Zhou, B., Rybski, D., Kropp, J.P., 2013. On the statistics of urban heat island intensity. Geophys. Res. Lett. 40, 5486–5491. https://doi.org/10.1002/2013GL057320.
Zhu, X., Chen, J., Gao, F., Chen, X., Masek, J.G., 2010. An enhanced spatial and temporal adaptive reflectance fusion model for complex heterogeneous regions. Remote Sens. Environ. 114, 2610–2623. https://doi.org/10.1016/j.rse.2010.05.032.
Zhu, X.X., Qiu, C., Hu, J., Shi, Y., Wang, Y., Schmitt, M., Taubenböck, H., 2022. The urban morphology on our planet – global perspectives from space. Remote Sens. Environ. 269, 112794 https://doi.org/10.1016/j.rse.2021.112794.
Ziaul, S., Pal, S., 2018. Analyzing control of respiratory particulate matter on land surface temperature in local climatic zones of English bazar municipality and surroundings. Urban Clim. 24, 34–50. https://doi.org/10.1016/j.uclim.2018.01.006.